Research Article Vol. 12, No. 3 / 1 March 2021 / Biomedical Optics Express 1437
Biomedical Optics EXPRESS

Label-free histological imaging of tissues using Brillouin light scattering contrast

SEUNGMI RYU,[1,2,5] NICOLA MARTINO,[1,5] SHELDON J. J. KWOK,[1,3] LIANE BERNSTEIN,[1,4] AND SEOK-HYUN YUN[1,3,*]

[1]Harvard Medical School and Wellman Center for Photomedicine, Massachusetts General Hospital, 65 Landsdowne St., Cambridge, MA 02139, USA
[2]National Center for Advancing Translational Sciences, National Institute of Health, Rockville, MD 20850, USA
[3]Harvard-MIT Health Sciences and Technology, Massachusetts Institute of Technology, Cambridge, MA 02139, USA
[4]Department of Electrical Engineering and Computer Science, Massachusetts Institute of Technology, Cambridge, MA 02139, USA
[5]These authors contributed equally to this work
*syun@hms.harvard.edu

Abstract: Brillouin light scattering offers a unique label-free approach to measure biomechanical properties non-invasively. While this technique is used in biomechanical analysis of cells and tissues, its potential for visualizing structural features of tissues based on the biomechanical contrast has not been much exploited. Here, we present high-resolution Brillouin microscopy images of four basic tissue types: muscular, connective, epithelial, and nervous tissues. The Brillouin contrast distinguishes between muscle fiber cells and endomysium in skeletal muscle and reveals chondrocytes along with spatially varying stiffness of the extracellular matrix in articular cartilage. The hydration-sensitive contrast can visualize the stratum corneum, epidermis, and dermis in the skin epithelium. In brain tissues, the Brillouin images show the mechanical heterogeneity across the cortex and deeper regions. This work demonstrates the versatility of using the Brillouin shift as histological contrast for examining intact tissue substructures via longitudinal modulus without the need for laborious tissue processing steps.

1. Introduction

Histological staining is a widely used method for examining the microscopic anatomy or structure of tissues. It involves fixation, embedding and sectioning, followed by staining with chemical coloring reagents or dye-conjugated antibodies against specific protein biomarkers. In the past decade, there have been efforts to exploit tissue-intrinsic optical contrasts, such as autofluorescence [1], second harmonic generation [2], infrared absorption [3], and stimulated Raman scattering [4], for histology. These label-free mechanisms can show tissue microstructures via differences in molecular compositions. These label-free imaging modalities have the potential as alternatives or supplements to conventional histological stains for tissue characterizations and pathological examinations.

The mechanical properties of tissues are intimately related to their microstructures and functions [5]. Changes in mechanical properties are associated with diseases, such as muscular dystrophy [6], osteoarthritis [7], and fibrosis [8]. Mechanical properties are also linked to fundamental biological processes, such as the deformation of cellular membrane integrity [9], changes in extracellular matrix (ECM) [7], and the disintegration of tissue architecture [10]. Mechanical characterization of tissues is therefore important in studying tissue development, homeostasis, and disease progression [11]. Histological staining can visualize structural proteins largely responsible for tissue stiffness such as collagen, elastin, glycosaminoglycan (GAG), and actin

#414474 https://doi.org/10.1364/BOE.414474
Journal © 2021 Received 12 Nov 2020; revised 3 Jan 2021; accepted 4 Jan 2021; published 17 Feb 2021

Biomedical Optics EXPRESS

fibers. However, neither histological staining nor the label-free imaging techniques listed above can provide quantitative mechanical information on a sample. A method that can visualize the mechanical properties of histological tissue samples could be useful in studies of mechanobiology and pathophysiology, as well as the diagnosis of diseases.

Brillouin light scattering microscopy is an optical technique capable of optically measuring the longitudinal elastic moduli of materials [12,13]. Brillouin scattering arises as photons are scattered by acoustic waves (phonons) present in a sample. The optical frequency shift, or the Brillouin shift ν_B, in the scattered photons carries information on the real part of the longitudinal modulus (M') of the material through the formula: $\nu_B = (2n/\lambda_0)\sqrt{M'/\rho}$ where λ_0 is the wavelength of the pump beam. In several biological materials the local refractive index (n) has been shown to scale approximately with the square root of the density (ρ), and variations in Brillouin shift can thus be generally interpreted as those of local longitudinal modulus [14] (with the only known exception of large lipid droplets [15]). However, as the exact quantitative relationship is expected to vary slightly depending on specific composition in tissue, in the following we report Brillouin shift values without extrapolating longitudinal moduli. Brillouin microscopy has recently been used to evaluate the biomechanical properties of various tissues [12,16–22], as the microscopic resolution and non-contact nature of this technique is well suited for histology, with an advantage over beads [23], atomic force microscopy [24], and elastography [25].

In this work, we demonstrate the potential for microscopic histological examinations of microstructures using the Brillouin shift as the contrast. As a proof of concept, we examine and discuss four examples of four major sub-types— muscular, connective, epithelial, and nervous tissues.

2. Results

2.1. Skeletal muscle tissue

The compliance of the muscular ECM affects its ability to sustain external loads during muscle contraction and prevents muscle tearing under external strains [26]. The viscoelastic property of the ECM changes with age and disease progression [27].

To test whether Brillouin microscopy can visualize the intact landscape of freshly isolated muscular tissues, we isolated tibialis anterior skeletal muscle from 6-week-old CD-1 mice and analyzed the transverse plane (x-z) of the muscle fascicles using confocal Brillouin microscopy (see Materials and methods). Histology using hematoxylin and eosin (H&E) and immunohistochemical staining against laminin [28] show the typical morphology of muscle fibers, basement membrane surrounding the fibers, and ECM known as the endomysium [29] between the fibers (Fig. 1(b)). In comparison, Brillouin microscopy images illustrate the distinct morphology of the muscle tissue in a label-free manner (Figs. 1(c) and S1). The muscle fibers exhibit considerably higher Brillouin shifts than their surrounding endomysium matrix. Variations of Brillouin shifts within individual muscle fibers are also noticeable, ranging from ~8.0-8.2 GHz.

2.2. Articular cartilage tissue

Articular cartilage is a representative load-bearing tissue, covering the ends of bones in joints. To obtain Brillouin images of articular cartilage, we used femoral articular cartilage obtained from a 9-month-old female New Zealand white rabbit (Fig. 2(a)). This connective tissue is divided into four distinct sub-layer zones [30]: the superficial, transitional, deep, and calcified zones. Histology of coronally-sectioned (x-z) cartilage stained with Masson's trichrome shows the sub-zones along the depth (Fig. 2(b)). Each zone features a unique cellular organization, ECM composition, water content, and mechanical properties (Fig. 2(c)) [31]. The superficial zone is a few tens of microns thick and has the highest cell population with flattened, disc-shaped

Biomedical Optics EXPRESS

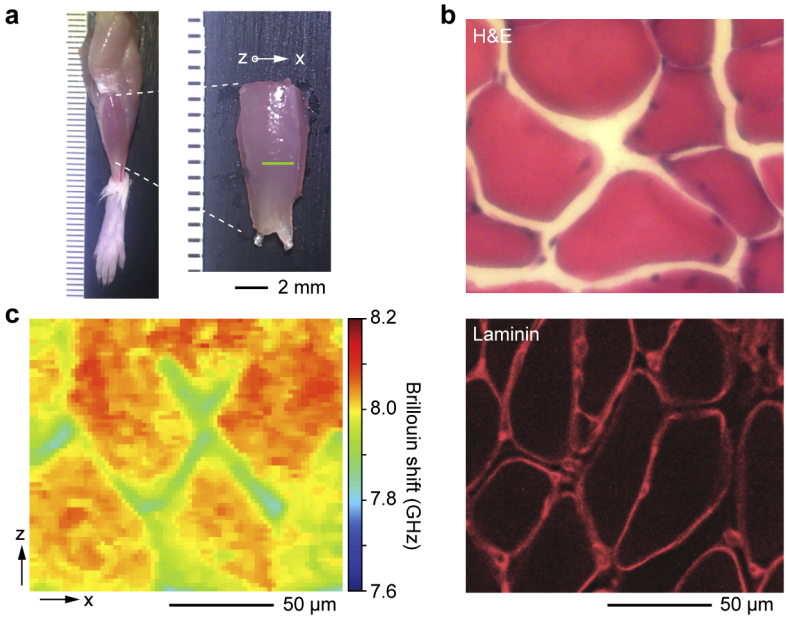

Fig. 1. Brillouin histology of skeletal muscle tissues. **a**, Image of the tibialis anterior skeletal muscle obtained from a 6-week old CD-1 female mouse. **b**, Histology sections of the tibialis anterior skeletal muscle after H&E staining (top) and immunostaining for laminin basement membrane protein (bottom). **c**, Brillouin shift map along an x-z plane of the intact muscle fascicle.

chondrocytes lying parallel to the surface. In the middle zone, the chondrocytes are rounder in shape. In the deep zone, the chondrocytes are larger, elongated, and distributed in vertical columnar arrays [32]. The ECM in the cartilage tissue is comprised of glycosaminoglycans (GAGs) and type II collagen, with an increasing trend of GAG and decreasing trend of collagen II from the superficial to the deep zone. The deep zone lacks type II collagen but is abundant with type X collagen. This ECM composition throughout the sub-zonal layer governs the water content and mechanical properties of the tissue, which play a central role in its function as cushioning layers in absorbing external shock.

Brillouin scans of femoral articular cartilage in the coronal plane showed distinct morphology of the superficial layer where cells were flattened and lying parallel to the surface (Figs. 2(d) and S2). The frequency shift of the ECM is much higher than that of chondrocytes, and it is higher in the transitional zone compared to the superficial zone (Fig. 2(e)), in accordance with previous studies showing increase in elastic modulus with depth [33]. The superficial layer is the most essential layer for the function of cartilage as the chondrocytes located within this zone produce a glycoprotein known as lubricin [34]. Lubricin is known as a critical protein that lubricates the joint system, thus preventing cartilage wear by reducing the friction coefficient of surface of articular cartilage [35]. During the onset and progression of injury and diseases such as osteoarthritis, the organization of the cartilage ECM, along with its mechanical modulus and water content, is altered [31,36]. Brillouin microscopy may thus potentially be useful as a tool to non-invasively characterize spatial pathological changes on injured cartilage.

Brillouin images of a transverse (x-y) plane clearly show chondrocytes in the cartilage ECM (Fig. 2(f)). This microstructure corresponds well to the histological image of a tissue section stained with toluidine blue (Fig. 2(g)), with pairs of chondrocytes divided from single progenitors with a thin ECM between the cells. An ECM with higher Brillouin shifts surrounds the

Biomedical Optics EXPRESS

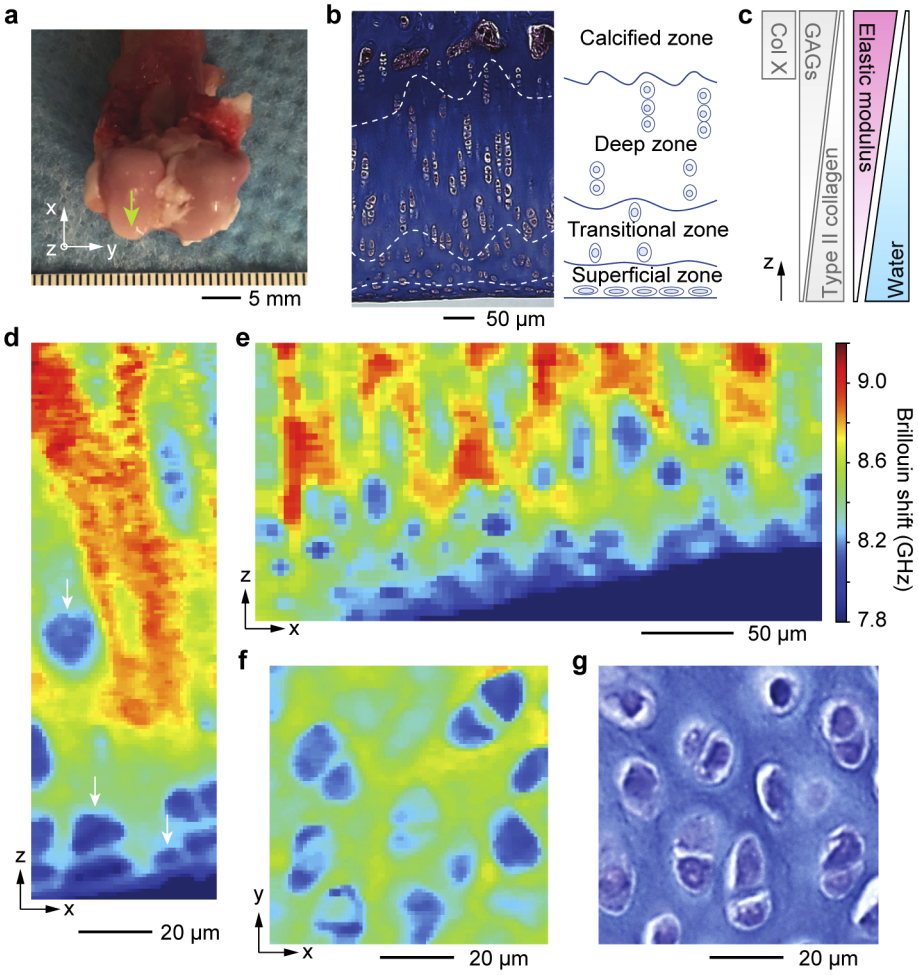

Fig. 2. Brillouin histology of articular cartilage tissues from 9-month-old female New Zealand white rabbit. **a**, Articular cartilage at the femoral head (arrow) was scanned with Brillouin microscopy followed by histological staining for a morphological comparison. **b**, Masson's trichrome staining image of a coronal section of the articular cartilage. Dashed lines and an anatomical schematic indicate the four sub-layer zones with chondrocytes. **c**, Spatial gradients of collagen and GAGs proteins, elastic modulus, and water content [31]. **d-e**, Brillouin images of an intact articular cartilage tissue in the x-z plane with high spatial resolution (d, 1 μm pixel size; e, 5 μm pixel size). Arrows indicate chondrocytes. ECM in the transitional zone has higher Brillouin shifts than that in the superficial zone. **f**, Brillouin image in the x-y plane at the transitional zone. Chondrocytes and the stiffer ECM are clearly distinguished. **g**, Toluidine blue stained image of a x-y cross-sectional tissue section of the transitional zone.

Biomedical Optics EXPRESS

chondrocyte clusters. While Brillouin shifts of the cells within skeletal muscle tissue and articular cartilage showed comparable shifts of ~8.0-8.2 GHz, Brillouin moduli of the ECM in muscle (~7.9 GHz) and cartilage (~8.3-9.2 GHz) could be distinguished.

2.3. Skin epithelial tissue

One of the essential functions of the epithelial tissues, such as the skin and cornea, is regulating water content. The hydration state of the skin is related to various dermatological problems and of great interest in the cosmetic industry as it affects the elasticity as well as appearance of the skin [37]. Corneal hydration is a critical factor in maintaining corneal transparency [38]. The Brillouin shift is sensitive to the corneal hydration state [39–41]. To evaluate how skin hydration affects the Brillouin shift, we imaged ear skin tissues biopsied from 6-week-old mice at three different conditions: normal fresh skin, dried skin (by applying warm air through incubation at 65 °C oven for 15 minutes), and pre-protected skin with petroleum jelly (Vaseline) followed by oven incubation. Vaseline is an occlusive moisturizer that reduces the rate of trans-epidermal water loss [42].

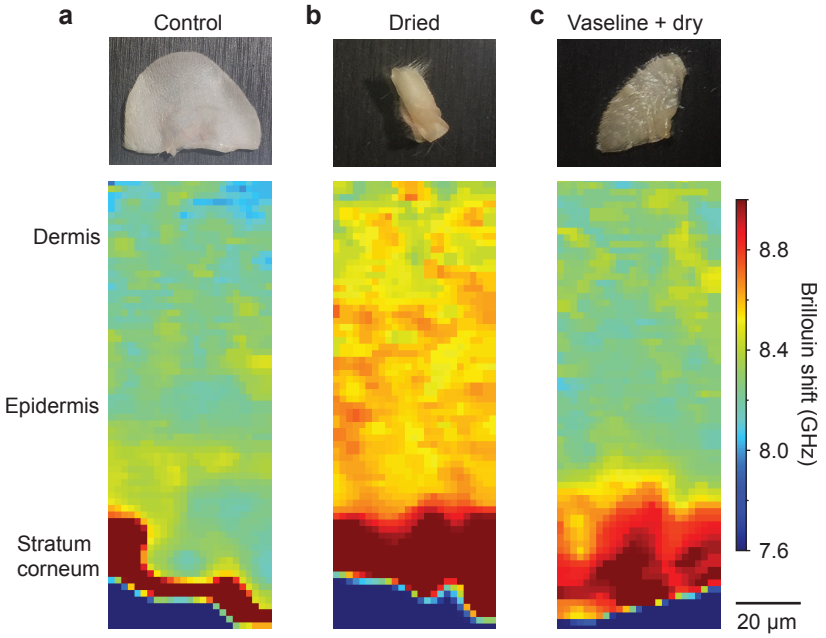

Fig. 3. Brillouin images of murine ear skin tissues: **a**, freshly biopsied; **b**, after drying; and **c**, drying after pre-treatment with Vaseline. Vaseline is shown to protect the epidermis and dermis from dehydration and also to cause swelling of the stratum corneum, as indicated by the increased thickness and increased Brillouin shift compared to the control.

Brillouin images reveal exceptionally high Brillouin shifts in the stratum corneum (Figs. 3(a) and S3a-c) with respect to the rest of the epidermis and dermis layers. This finding is consistent with the low water content in the outermost, dehydrated layer of the skin, where a higher elastic modulus implies a larger Brillouin shift [43]. Compared to the normal skin, dried skin showed an extension of the dehydrated region beyond the stratum corneum and an overall increase in Brillouin shift in the epidermis and dermis regions (Figs. 3(b) and S3d-f). By contrast, the same drying condition on the skin after Vaseline pre-treatment reduced the change in Brillouin shift in the dermis (Figs. 3(c) and S3g-i). The observed thickening of the top region with high Brillouin

Biomedical Optics EXPRESS

shifts is attributed to the swelling of the stratum corneum due to the Vaseline [42]. These results suggest the potential applications of Brillouin microscopy for investigating the hydration status across various skin sub-layers at high resolution.

2.4. Brain tissue

The viscoelastic modulus of brain tissues is an important factor in neuronal development, traumatic injury, and pathology. During development, mechanical cues modulate the growth of neurites and differentiation of precursor cells [44–46], as well as the interactions between neurons and glial cells [47]. The stiffness of brain sub-regions influences how external physical impacts exert stress and strain on brain cells. Typically, cellular damage is more evident in regions with lower elastic modulus [48,49]. Also, pathological process in the brain often involves activation of astrocytes, resulting in stiff scar tissues that may be a major impediment to regeneration of neural networks [50–52].

To map the mechanical properties of brain tissues by Brillouin microscopy, we prepared coronal sections of brain tissues obtained from 6-week-old female mice. The anatomic regions of interest analyzed in this study include grey matter (cerebral cortex, putamen, and hippocampus) and white matter (corpus callosum) (Fig. 4(a)) [53]. Brillouin images revealed heterogeneous frequency shift values in both microscopic and macroscopic length scales (Figs. 4(b), 4(c) and S4). The cortex and putamen, which are mainly populated by neuronal cells [53], showed low

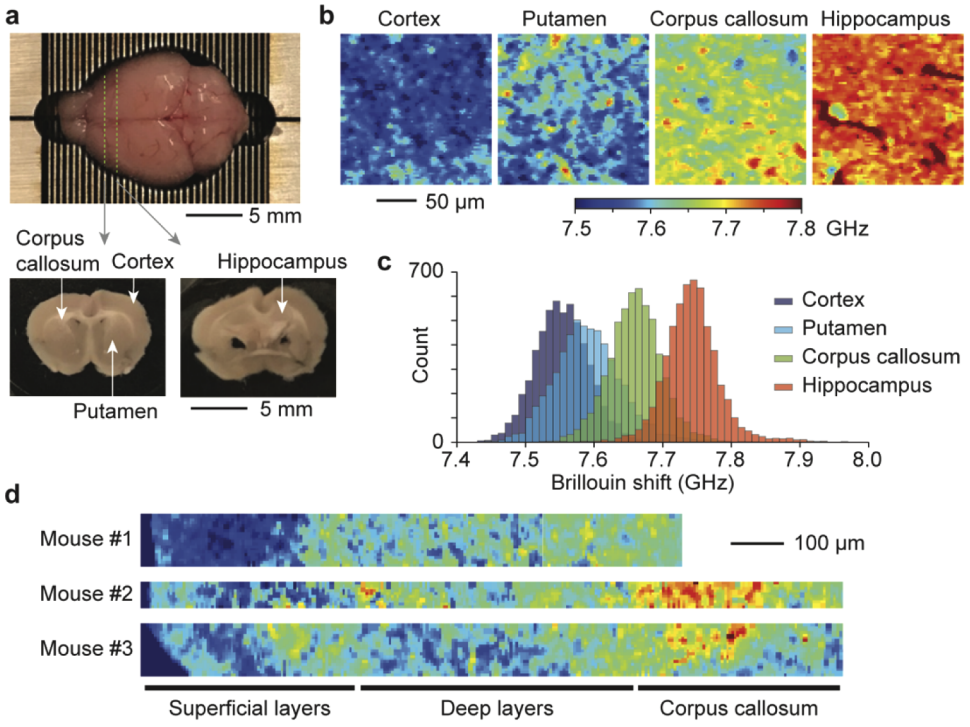

Fig. 4. Brillouin images of brain tissue slices. **a**, Coronal brain slices obtained from a 6-week old CD-1 female mouse at -1 and -2 mm from the bregma. **b**, Brillouin images taken at a depth of 50 μm from the tissue surface at four anatomically distinct sites: cortex, putamen, corpus callosum, and hippocampus. **c**, Histogram of Brillouin shifts in the four different regions. **d**, Brillouin maps of brain tissue slices from three different mice taken across the sub-cortical layers and corpus callosum.

Biomedical Optics EXPRESS

Brillouin shifts. The corpus callosum exhibited higher mean Brillouin shift, presumably due to high concentration of glial cells and a dense network of lipid-rich myelinated axons [54–56]. The hippocampus, which contains laminated and tightly oriented neuronal bodies [57], had the highest mean Brillouin shifts. These measurements are in accordance with a previous report that the hippocampus showed significantly higher elastic modulus than the cortex and corpus callosum [58].

The cerebral cortex consists of six radial layers. Each cortical layer contains different functional neuronal types, organizations, and densities. Broadly, these layers can be categorized into superficial layers (I-III) and deep layers (IV-VI). The deep layers contain large pyramidal cells with more densely myelinated axons than the superficial layers [59]. Brillouin maps along the cortex showed that the deeper layers had a higher mean Brillouin shift compared to the superficial layers, and those results were reproducible across the neocortex from different mice of the same age (Fig. 4(d)). The results demonstrated the ability of Brillouin microscopy to visualize the heterogeneous mechanical properties of brain tissues.

3. Discussion

To compare different tissue types, we plot the Brillouin shifts measured from various tissues including ocular tissues previously measured using the same instrument [39,60,61]. To facilitate comparisons with data from literature, we use a normalized scale [62] relative to water given by: $\frac{\nu_B(\text{tissue})-\nu_B(\text{water})}{\nu_B(\text{water})}$. This metric indicates the contribution of solid substances in the tissue to the Brillouin shift and is nearly independent of the optical wavelength used. The different brain regions show the lowest average frequency shift, followed by muscle, skin and cartilage, with all values in the range 7.5 - 9.0 GHz.

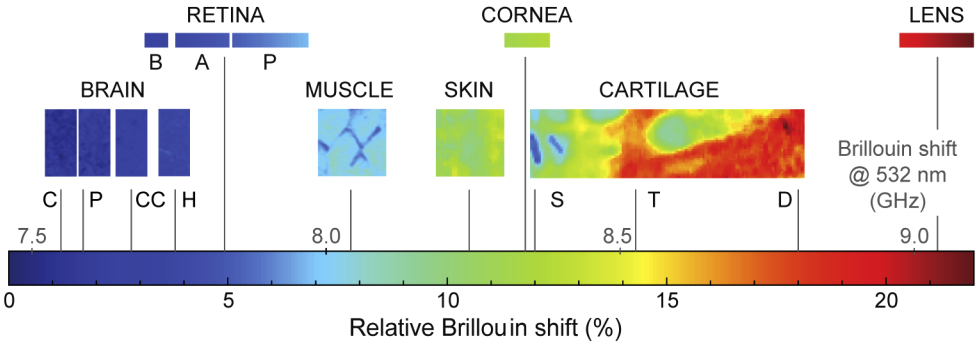

Fig. 5. The range of range of Brillouin shift values for various tissues. The brain (C: cortex, P: putamen, CC: corpus callosum, H: hippocampus), muscle, skin, and cartilage (S: superficial, T: transitional, D: deep) data were obtained in this work. Literature data were used for porcine retina (B, basal: nerve fiber layer, retinal ganglion cell layer, inner plexiform layer; A, apical: inner nuclear layer, outer plexiform layer, P, photoreceptor cell layer: outer nuclear layer, photoreceptor inner segment, photoreceptor outer segment) from Ref. [60]; human cornea from Ref. [39]; human crystalline lens from Ref. [61].

Brillouin microscopy is sensitive to the water content of biological materials. As detailed in Ref. [63], using a concentration-weighted sum approximation, the contributions to the change in Brillouin shift from water content (ε_f) and changes in compressibility of the solid fraction (β_s) can be approximated as: $\frac{\Delta\nu_B}{\nu_B} \approx -0.4\frac{\Delta\varepsilon_f}{\varepsilon_f} - 0.04\frac{\Delta\beta_s}{\beta_s}$. Indeed, we can observe a similar trend between the average Brillouin shifts of the tissues measured here and their water content, as found in literature (brain: 82 - 85%, muscle: 73 - 78%, skin: 60 - 76%, cartilage: 65 - 80% [64,65]). However, water content alone is not sufficient to explain the observed variations in Brillouin shift

Biomedical Optics EXPRESS

[62]. A change in water content from brain to cartilage of 20% would contribute to a change in Brillouin frequency of about 8%, i.e. 0.6 - 0.7 GHz for the values in our ranges, roughly half of the actual variation observed. We can thus ascribe the remaining change in Brillouin shifts to contributions from the solid part of tissue.

The observed trend is also in good agreement with the data from ocular tissues. The retina, which is made up of nervous tissue, has relative Brillouin shifts comparable to those observed in the brain. The stroma of the cornea, which is main component of the cornea, contains collagen, GAG, and corneal fibroblasts called the keratocytes [66]. Such components resemble those of the dermis layer of the skin, and thus have similar relative Brillouin shifts. The crystalline lens of the eye is well-known to have a much higher protein content than other tissue parts in the body, up to 60% of its total mass [67]. Tight packing of these proteins leads to its high stiffness and transparency [68]. Such unique biological properties are reflected in the high Brillouin shift of the lens, which shows the highest value among all the tissues investigated.

The measurement error in the frequency shift measurement was about 10-20 MHz (standard error, see maps in Supplement 1). The uncertainty increases at deeper imaging depth in tissues due to a decrease in signal-to-noise ratio caused by scattering. This limited our current penetration depths to about 100 µm. The use of a red or near-infrared (NIR) laser wavelength and higher optical power can increase the penetration depth.

Brillouin microscopy can also provide information on the imaginary part of the longitudinal modulus (related to material viscosity) from the measurement of the Brillouin spectral linewidth [12]. However, the finite numerical aperture (NA) of the objective lens used and the finite instrument resolution must be taken into account in the linewidth measurement.

In the current study, the input laser beam has a circular polarization state. Tissues with aligned structures, like collagen fibers or muscle fibrils, may exhibit direction-dependent, or anisotropic, mechanical properties. It may be possible to measure the anisotropic properties by using linear input polarization states and analyzing polarization-dependent Brillouin shifts.

The measurements presented here were taken on fresh, unprocessed tissues without any fixation, sucrose immersion, or dehydration/rehydration steps. While this method is desirable to avoid any processing-induced change in the Brillouin shift of the tissue and also to greatly reduce sample preparation time, fixation may be necessary in routine histological analysis when samples cannot be immediately measured after collection. For such applications, additional studies are needed to identify specific fixation protocols that minimize artificial changes in the Brillouin shift.

In conclusion, we have demonstrated high-resolution histological maps of bulk unprocessed tissues of four different tissue subtypes using Brillouin shift as indigenous contrast. Brillouin microscopy reveals the microscopically and macroscopically heterogenous mechanical properties across cells, ECM and sub-regions within tissues. Label-free histological examinations of tissue modulus by Brillouin microscopy could be useful in various investigational and diagnostic applications.

4. Materials and methods

Brillouin imaging. Brillouin imaging was done on a custom-modified inverted microscope (Olympus IX-71). A 532 nm continuous-wave laser (Laser Quantum Torus 532) was coupled to the microscope via the right-side port and focused onto the sample with a 40X objective (Olympus LUCPlanFLN 40X). The laser power at the sample plane was ~2-4 mW. The Brillouin scattered light was collected by the objective and, after passing through a 90:10 beam-splitter, was coupled to a single-mode optical fiber serving as a confocal pinhole. The fiber output was transmitted through a two-stage VIPA spectrometer (FSR 30 GHz, Light Machinery) [69] with a Lyot stop for enhanced background noise rejection [70]. The Brillouin signal was acquired with an electron-multiplying charge-coupled device (EM-CCD) camera (Andor iXon). Brillouin imaging was performed by raster scanning the sample with a motorized stage and acquiring a

Biomedical Optics EXPRESS

spectrum at each pixel with an integration time between 150-300 ms. Before each scan, the system was calibrated by acquiring the Brillouin signal from a reference sample (interface between water and a poly(methyl methacrylate) cuvette), controlled for temperature. The raw data from the spectrometer was analyzed with custom code written in Python using the *SciPy* library [71]. For each pixel, the algorithm extracts the Brillouin spectrum from the image acquired by the camera by summing the data from 9 lines around the highest-intensity line. The Stokes and anti-Stokes peaks are then fitted with Lorentzian line-shapes to extract their central position and the Brillouin shift is finally calculated as the average of their absolute values. Representative spectra for each tissue type are reported in Supplement 1, along with maps of peak linewidths and estimates for the uncertainty of the Brillouin shifts obtained from fitting. The 2D Brillouin maps are finally post-processed with a 3-pixel square median filter.

Tissue preparation. For muscle, skin, and brain tissue imaging, fresh tissues were collected from 6-week old female CD-1 mice (Charles River Laboratories, USA). For articular cartilage tissue imaging, fresh legs with an intact femoral head were obtained from 9-month-old female New Zealand white rabbits that were sacrificed in another experimental protocol and used within 4 hours of death. The Massachusetts General Hospital Institutional Animal Care and Use Committee (IACUC) approved all animal study procedures (Protocol ID 2016N000056). Euthanasia of mice was performed by decapitation with a commercially available guillotine (Kent Scientific, USA). Following euthanasia, either brain, tibialis anterior muscle, or ear with intact skin was harvested to investigate under Brillouin microscope. For skin tissue imaging, an ear with intact skin was examined right after incision for investigation of normal skin condition. For the study of the dried skin condition, bare skin and skin applied with Vaseline (Sigma Aldrich, USA) were placed in a drying oven chamber at 65 °C for 15 minutes. For brain tissue imaging, the brain was explanted from the skull and cut into 1-mm-thick slices in the coronal plane with a stainless-steel adult mouse brain slicer (Zivic Instruments, USA) -1 mm from the bregma to scan the corpus callosum, cortex, and putamen, and -2 mm from the bregma to scan the hippocampus. All tissue samples were contained in sterile glass-bottom tissue culture plates (Cellvis, USA) immersed with either phosphate buffer saline (Gibco, USA) for muscle, skin, and cartilage, or artificial cerebrospinal fluid (Tocris, USA) for brain tissue to maintain the tissue viability and integrity during testing.

H&E histology and Immunohistochemistry. The harvested tibialis anterior muscle from mouse and femoral head tissues from the rabbit joint were immersed in a 10% neutral buffered formalin solution (Sigma Aldrich, USA). Muscle tissues were immersed in 30% sucrose solution (Sigma Aldrich, USA) for cryoprotection, embedded in optimal cutting temperature compound (Fisher scientific, USA), and sectioned at a thickness of 10 μm. The sections were stained with the hematoxylin and eosin (H&E) staining method and observed under a light microscope (IX71 inverted microscope, Olympus). The sections were immuno-stained with antibodies against laminin (Abcam, USA). The immunostaining signal was detected with rhodamine isothiocyanate-conjugated secondary antibodies (Jackson ImmunoResearch Laboratories, USA). Following fixation, femoral head tissues were decalcified in Decalcifying Solution-Lite (Sigma Aldrich, USA), dehydrated in increasing concentrations of ethanol (Sigma Aldrich, USA), and embedded in paraffin (Sigma Aldrich, USA). The paraffin-embedded tissues were sectioned either coronally or transversely at a thickness of 4 μm. The tissues underwent deparaffinization and hydration steps using xylene and decreasing concentrations of ethanol. The hydrated tissues were stained with either H&E, Masson's trichrome, or Toluidine blue staining method. Following staining, the tissues were dehydrated with increasing concentrations of ethanol, xylene, and were mounted with Canada Balsam (Sigma Aldrich, USA).

Funding. National Science Foundation (CMMI-1562863); National Institutes of Health (P41EB015903, R01CA192878, R01EB027653, R01EY025454); Korea Institute of Science and Technology (2E27830, 2E27833); National Research Foundation of Korea (2017R1A6A3A03004304).

Biomedical Optics EXPRESS

Disclosures. SHY: Intelon Optics (F,P).

See Supplement 1 for supporting content.

References

1. Y. Rivenson, H. Wang, Z. Wei, K. de Haan, Y. Zhang, Y. Wu, H. Günaydın, J. E. Zuckerman, T. Chong, A. E. Sisk, L. M. Westbrook, W. D. Wallace, and A. Ozcan, "Virtual histological staining of unlabelled tissue-autofluorescence images via deep learning," Nat. Biomed. Eng. **3**(6), 466–477 (2019).
2. H. Tu, Y. Liu, D. Turchinovich, M. Marjanovic, J. K. Lyngsø, J. Lægsgaard, E. J. Chaney, Y. Zhao, S. You, W. L. Wilson, B. Xu, M. Dantus, and S. A. Boppart, "Stain-free histopathology by programmable supercontinuum pulses," Nat. Photonics **10**(8), 534–540 (2016).
3. M. Schnell, S. Mittal, K. Falahkheirkhah, A. Mittal, K. Yeh, S. Kenkel, A. Kajdacsy-Balla, P. S. Carney, and R. Bhargava, "All-digital histopathology by infrared-optical hybrid microscopy," Proc. Natl. Acad. Sci. **117**(7), 3388–3396 (2020).
4. T. C. Hollon, B. Pandian, A. R. Adapa, E. Urias, A. V. Save, S. S. S. Khalsa, D. G. Eichberg, R. S. D'Amico, Z. U. Farooq, S. Lewis, P. D. Petridis, T. Marie, A. H. Shah, H. J. L. Garton, C. O. Maher, J. A. Heth, E. L. McKean, S. E. Sullivan, S. L. Hervey-Jumper, P. G. Patil, B. G. Thompson, O. Sagher, G. M. McKhann, R. J. Komotar, M. E. Ivan, M. Snuderl, M. L. Otten, T. D. Johnson, M. B. Sisti, J. N. Bruce, K. M. Muraszko, J. Trautman, C. W. Freudiger, P. Canoll, H. Lee, S. Camelo-Piragua, and D. A. Orringer, "Near real-time intraoperative brain tumor diagnosis using stimulated Raman histology and deep neural networks," Nat. Med. **26**(1), 52–58 (2020).
5. C. F. Guimarães, L. Gasperini, A. P. Marques, and R. L. Reis, "The stiffness of living tissues and its implications for tissue engineering," Nat. Rev. Mater. **5**(5), 351–370 (2020).
6. L. Lacourpaille, F. Hug, A. Guével, Y. Péréon, A. Magot, J.-Y. Hogrel, and A. Nordez, "Non-invasive assessment of muscle stiffness in patients with duchenne muscular dystrophy," Muscle Nerve **51**(2), 284–286 (2015).
7. L. Han, A. J. Grodzinsky, and C. Ortiz, "Nanomechanics of the cartilage extracellular matrix," Annu. Rev. Mater. Res. **41**(1), 133–168 (2011).
8. B. Hinz, "Tissue stiffness, latent TGF-β1 Activation, and mechanical signal transduction: Implications for the pathogenesis and treatment of fibrosis," Curr. Rheumatol. Rep. **11**(2), 120–126 (2009).
9. J. A. Goldstein and E. M. McNally, "Mechanisms of muscle weakness in muscular dystrophy," The Journal of General Physiology **136**(1), 29–34 (2010).
10. C. T. McKee, J. A. Last, P. Russell, and C. J. Murphy, "Indentation versus tensile measurements of Young's Modulus for soft biological tissues," Tissue Eng., Part B **17**(3), 155–164 (2011).
11. A. M. Handorf, Y. Zhou, M. A. Halanski, and W.-J. Li, "Tissue stiffness dictates development, homeostasis, and disease progression," Organogenesis **11**(1), 1–15 (2015).
12. G. Scarcelli and S. H. Yun, "Confocal Brillouin microscopy for three-dimensional mechanical imaging," Nat. Photonics **2**(1), 39–43 (2008).
13. G. Scarcelli, W. J. Polacheck, H. T. Nia, K. Patel, A. J. Grodzinsky, R. D. Kamm, and S. H. Yun, "Noncontact three-dimensional mapping of intracellular hydromechanical properties by Brillouin microscopy," Nat. Methods **12**(12), 1132–1134 (2015).
14. R. Prevedel, A. Diz-Muñoz, G. Ruocco, and G. Antonacci, "Brillouin microscopy: an emerging tool for mechanobiology," Nat. Methods **16**(10), 969–977 (2019).
15. R. Schlüßler, K. Kim, M. Nötzel, A. Taubenberger, S. Abuhattum, T. Beck, P. Müller, S. Maharana, G. Cojoc, S. Girardo, A. Hermann, S. Alberti, and J. Guck, "Combined fluorescence, optical diffraction tomography and Brillouin microscopy," bioRxiv 2020.10.30.361808 (2020).
16. C. Poon, J. Chou, M. Cortie, and I. Kabakova, "Brillouin imaging for studies of micromechanics in biology and biomedicine: from current state-of-the-art to future clinical translation," (2020).
17. G. Scarcelli, R. Pineda, and S. H. Yun, "Brillouin optical microscopy for corneal biomechanics," Invest. Ophthalmol. Visual Sci. **53**(1), 185 (2012).
18. V. Mathieu, K. Fukui, M. Matsukawa, M. Kawabe, R. Vayron, E. Soffer, F. Anagnostou, and G. Haiat, "Micro-Brillouin scattering measurements in mature and newly formed bone tissue surrounding an implant," J. Biomech. Eng. **133**(2), 1–6 (2011).
19. F. Palombo, M. Madami, N. Stone, and D. Fioretto, "Mechanical mapping with chemical specificity by confocal Brillouin and Raman microscopy," Analyst **139**(4), 729–733 (2014).
20. F. Palombo, M. Madami, D. Fioretto, J. Nallala, H. Barr, A. David, and N. Stone, "Chemico-mechanical imaging of Barrett's oesophagus," J. Biophotonics **9**(7), 694–700 (2016).
21. R. Raghunathan, J. Zhang, C. Wu, J. Rippy, and M. Singh, "Evaluating biomechanical properties of murine embryos using Brillouin microscopy and optical coherence tomography," J. Biomed. Opt. **22**(08), 1 (2017).
22. J. Zhang, R. Raghunathan, J. Rippy, C. Wu, R. H. Finnell, K. V. Larin, and G. Scarcelli, "Tissue biomechanics during cranial neural tube closure measured by Brillouin microscopy and optical coherence tomography," Birth Defects Res. **111**(14), 991–998 (2019).
23. P. H. Wu, D. R. Ben Aroush, A. Asnacios, W. C. Chen, M. E. Dokukin, B. L. Doss, P. Durand-Smet, A. Ekpenyong, J. Guck, N. V. Guz, P. A. Janmey, J. S. H. Lee, N. M. Moore, A. Ott, Y. C. Poh, R. Ros, M. Sander, I. Sokolov, J. R. Staunton, N. Wang, G. Whyte, and D. Wirtz, "A comparison of methods to assess cell mechanical properties," Nat. Methods **15**(7), 491–498 (2018).

Biomedical Optics EXPRESS

24. M. Krieg, G. Fläschner, D. Alsteens, B. M. Gaub, W. H. Roos, G. J. L. Wuite, H. E. Gaub, C. Gerber, Y. F. Dufrêne, and D. J. Müller, "Atomic force microscopy-based mechanobiology," Nat. Rev. Phys. **1**(1), 41–57 (2019).
25. B. F. Kennedy, P. Wijesinghe, and D. D. Sampson, "The emergence of optical elastography in biomedicine," Nat. Photonics **11**(4), 215–221 (2017).
26. G. A. Meyer and R. L. Lieber, "Elucidation of extracellular matrix mechanics from muscle fibers and fiber bundles," Journal of Biomechanics **44**(4), 771–773 (2011).
27. L. K. Wood, E. Kayupov, J. P. Gumucio, C. L. Mendias, D. R. Claflin, and S. V. Brooks, "Intrinsic stiffness of extracellular matrix increases with age in skeletal muscles of mice," J. Appl. Physiol. **117**(4), 363–369 (2014).
28. J. Holmberg and M. Durbeej, "Laminin-211 in skeletal muscle function," Cell Adhes. Migr. **7**(1), 111–121 (2013).
29. A. R. Gillies and R. L. Lieber, "Structure and function of the skeletal muscle extracellular matrix," Muscle Nerve **44**(3), 318–331 (2011).
30. A. R. Poole, T. Kojima, T. Yasuda, F. Mwale, M. Kobayashi, and S. Laverty, "Composition and structure of articular cartilage," Clin. Orthop. Relat. Res. **391**(391 Suppl), S26–S33 (2001).
31. L. H. Nguyen, A. K. Kudva, N. S. Saxena, and K. Roy, "Engineering articular cartilage with spatially-varying matrix composition and mechanical properties from a single stem cell population using a multi-layered hydrogel," Biomaterials **32**(29), 6946–6952 (2011).
32. J. S. Temenoff and A. G. Mikos, "Review: tissue engineering for regeneration of articular cartilage," Biomaterials **21**(5), 431–440 (2000).
33. J. Antons, M. G. M. Marascio, J. Nohava, R. Martin, L. A. Applegate, P. E. Bourban, and D. P. Pioletti, "Zone-dependent mechanical properties of human articular cartilage obtained by indentation measurements," J. Mater. Sci.: Mater. Med. **29**(5), 57 (2018).
34. M. B. Albro, M. S. Bergholt, J. P. St-Pierre, A. Vinals Guitart, H. M. Zlotnick, E. G. Evita, and M. M. Stevens, "Raman spectroscopic imaging for quantification of depth-dependent and local heterogeneities in native and engineered cartilage," npj Regener. Med. **3**(1), 3 (2018).
35. G. Musumeci, "The role of lubricin in normal and pathological joint tissue: A contemporary review," OA Anat. **1**(1), 1–6 (2013).
36. P.-J. Wu, M. I. Masouleh, D. Dini, C. Paterson, P. Török, D. R. Overby, and I. V. Kabakova, "Detection of proteoglycan loss from articular cartilage using Brillouin microscopy, with applications to osteoarthritis," Biomed. Opt. Express **10**(5), 2457 (2019).
37. E. H. Mojumdar, Q. D. Pham, D. Topgaard, and E. Sparr, "Skin hydration: interplay between molecular dynamics, structure and water uptake in the stratum corneum," Sci. Rep. **7**(1), 15712 (2017).
38. G. B. Benedek, "Theory of Transparency of the Eye," Appl. Opt. **10**(3), 459 (1971).
39. P. Shao, T. G. Seiler, A. M. Eltony, A. Ramier, S. J. J. Kwok, G. Scarcelli, R. P. Li, and S.-H. Yun, "Effects of Corneal Hydration on Brillouin Microscopy In Vivo," Invest. Ophthalmol. Visual Sci. **59**(7), 3020 (2018).
40. G. Scarcelli, S. Besner, R. Pineda, P. Kalout, and S. H. Yun, "In vivo biomechanical mapping of normal and keratoconus corneas," JAMA Ophthalmol. **133**(4), 480 (2015).
41. A. M. Eltony, F. Clouser, P. Shao, R. Pineda, and S.-H. Yun, "Brillouin microscopy visualizes centralized corneal edema in fuchs endothelial dystrophy," Cornea **39**(2), 168–171 (2020).
42. F. Mirrashed and J. C. Sharp, "In vivo quantitative analysis of the effect of hydration (immersion and Vaseline treatment) in skin layers using high-resolution MRI and magnetisation transfer contrast*," Skin Research and Technology **10**(1), 14–22 (2004).
43. Y. Hara, Y. Masuda, T. Hirao, and N. Yoshikawa, "The relationship between the Young's modulus of the stratum corneum and age: a pilot study," Skin Research and Technology **19**(3), 339–345 (2013).
44. K. Franze and J. Guck, "The biophysics of neuronal growth," Rep. Prog. Phys. **73**(9), 094601 (2010).
45. K. Saha, A. J. Keung, E. F. Irwin, Y. Li, L. Little, D. V. Schaffer, and K. E. Healy, "Substrate modulus directs neural stem cell behavior," Biophys. J. **95**(9), 4426–4438 (2008).
46. N. D. Leipzig and M. S. Shoichet, "The effect of substrate stiffness on adult neural stem cell behavior," Biomaterials **30**(36), 6867–6878 (2009).
47. P. C. Georges, W. J. Miller, D. F. Meaney, E. S. Sawyer, and P. A. Janmey, "Matrices with compliance comparable to that of brain tissue select neuronal over glial growth in mixed cortical cultures," Biophys. J. **90**(8), 3012–3018 (2006).
48. B. S. Elkin, A. I. Ilankovan, and B. Morrison, "A detailed viscoelastic characterization of the P17 and adult rat brain," Journal of Neurotrauma **28**(11), 2235–2244 (2011).
49. T. Igarashi, M. B. Potts, and L. J. Noble-Haeusslein, "Injury severity determines Purkinje cell loss and microglial activation in the cerebellum after cortical contusion injury," Exp. Neurol. **203**(1), 258–268 (2007).
50. A. Buffo, C. Rolando, and S. Ceruti, "Astrocytes in the damaged brain: Molecular and cellular insights into their reactive response and healing potential," Biochem. Pharmacol. **79**(2), 77–89 (2010).
51. A. Sandvig, M. Berry, L. B. Barrett, A. Butt, and A. Logan, "Myelin-, reactive glia-, and scar-derived CNS axon growth inhibitors: Expression, receptor signaling, and correlation with axon regeneration," Glia **46**(3), 225–251 (2004).
52. M. Pekny, U. Wilhelmsson, and M. Pekna, "The dual role of astrocyte activation and reactive gliosis," Neurosci. Lett. **565**, 30–38 (2014).
53. J. Sun, S. J. Lee, L. Wu, M. Sarntinoranont, and H. Xie, "Refractive index measurement of acute rat brain tissue slices using optical coherence tomography," Opt. Express **20**(2), 1084 (2012).

Biomedical Optics EXPRESS

54. M. A. Green, L. E. Bilston, and R. Sinkus, "In vivo brain viscoelastic properties measured by magnetic resonance elastography," NMR Biomed. **21**(7), 755–764 (2008).
55. J. Weickenmeier, R. de Rooij, S. Budday, P. Steinmann, T. C. Ovaert, and E. Kuhl, "Brain stiffness increases with myelin content," Acta Biomater. **42**, 265–272 (2016).
56. M. Troyanova-Wood, Z. Coker, A. Traverso, and V. V. Yakovlev, "Using Brillouin microspectroscopy to characterize adipocytes' response to lipid droplet accumulation," in *Proc. SPIE*, K. V. Larin and D. D. Sampson, eds. (2017), 10067, p. 100670K.
57. E. Förster, S. Zhao, and M. Frotscher, "Laminating the hippocampus," Nat. Rev. Neurosci. **7**(4), 259–268 (2006).
58. J. D. Finan, B. S. Elkin, E. M. Pearson, I. L. Kalbian, and B. Morrison, "Viscoelastic properties of the rat brain in the sagittal plane: effects of anatomical structure and age," Ann. Biomed. Eng. **40**(1), 70–78 (2012).
59. G. S. Tomassy, D. R. Berger, H.-H. Chen, N. Kasthuri, K. J. Hayworth, A. Vercelli, H. S. Seung, J. W. Lichtman, and P. Arlotta, "Distinct profiles of myelin distribution along single axons of pyramidal neurons in the neocortex," Science **344**(6181), 319–324 (2014).
60. I. P. Weber, S. H. Yun, G. Scarcelli, and K. Franze, "The role of cell body density in ruminant retina mechanics assessed by atomic force and Brillouin microscopy," Phys. Biol. **14**(6), 065006 (2017).
61. S. Besner, G. Scarcelli, R. Pineda, and S.-H. Yun, "In vivo Brillouin analysis of the aging crystalline lens," Invest. Ophthalmol. Visual Sci. **57**(13), 5093 (2016).
62. G. Antonacci, T. Beck, A. Bilenca, J. Czarske, K. Elsayad, J. Guck, K. Kim, B. Krug, F. Palombo, R. Prevedel, and G. Scarcelli, "Recent progress and current opinions in Brillouin microscopy for life science applications," Biophys. Rev. **12**(3), 615–624 (2020).
63. G. Scarcelli and S. H. Yun, "Reply to 'Water content, not stiffness, dominates Brillouin spectroscopy measurements in hydrated materials'," Nat. Methods **15**(8), 562–563 (2018).
64. R. Pethig and D. B. Kell, "The passive electrical properties of biological systems: their significance in physiology, biophysics and biotechnology," Phys. Med. Biol. **32**(8), 933–970 (1987).
65. J. A. Buckwalter and H. J. Mankin, "Instructional Course Lectures, The American Academy of Orthopaedic Surgeons - Articular Cartilage. Part I," J. Bone Jt. Surg. **79**(4), 600–611 (1997).
66. M. J. Doughty and M. L. Zaman, "Human Corneal Thickness and Its Impact on Intraocular Pressure Measures," Surv. Ophthalmol. **44**(5), 367–408 (2000).
67. M. Ireland and H. Maisel, "A family of lens fiber cell specific proteins," Lens and eye toxicity research **6**(4), 623–638 (1989).
68. M. Delaye and A. Tardieu, "Short-range order of crystallin proteins accounts for eye lens transparency," Nature **302**(5907), 415–417 (1983).
69. G. Scarcelli and S. H. Yun, "Multistage VIPA etalons for high-extinction parallel Brillouin spectroscopy," Opt. Express **19**(11), 10913 (2011).
70. E. Edrei, M. C. Gather, and G. Scarcelli, "Integration of spectral coronagraphy within VIPA-based spectrometers for high extinction Brillouin imaging," Opt. Express **25**(6), 6895 (2017).
71. P. Virtanen, R. Gommers, T. E. Oliphant, M. Haberland, T. Reddy, D. Cournapeau, E. Burovski, P. Peterson, W. Weckesser, J. Bright, S. J. van der Walt, M. Brett, J. Wilson, K. J. Millman, N. Mayorov, A. R. J. Nelson, E. Jones, R. Kern, E. Larson, C. J. Carey, İ. Polat, Y. Feng, E. W. Moore, J. VanderPlas, D. Laxalde, J. Perktold, R. Cimrman, I. Henriksen, E. A. Quintero, C. R. Harris, A. M. Archibald, A. H. Ribeiro, F. Pedregosa, P. van Mulbregt, A. Vijaykumar, A. pietro Bardelli, A. Rothberg, A. Hilboll, A. Kloeckner, A. Scopatz, A. Lee, A. Rokem, C. N. Woods, C. Fulton, C. Masson, C. Häggström, C. Fitzgerald, D. A. Nicholson, D. R. Hagen, D. V. Pasechnik, E. Olivetti, E. Martin, E. Wieser, F. Silva, F. Lenders, F. Wilhelm, G. Young, G. A. Price, G. L. Ingold, G. E. Allen, G. R. Lee, H. Audren, I. Probst, J. P. Dietrich, J. Silterra, J. T. Webber, J. Slavič, J. Nothman, J. Buchner, J. Kulick, J. L. Schönberger, J. V. de Miranda Cardoso, J. Reimer, J. Harrington, J. L. C. Rodríguez, J. Nunez-Iglesias, J. Kuczynski, K. Tritz, M. Thoma, M. Newville, M. Kümmerer, M. Bolingbroke, M. Tartre, M. Pak, N. J. Smith, N. Nowaczyk, N. Shebanov, O. Pavlyk, P. A. Brodtkorb, P. Lee, R. T. McGibbon, R. Feldbauer, S. Lewis, S. Tygier, S. Sievert, S. Vigna, S. Peterson, S. More, T. Pudlik, T. Oshima, T. J. Pingel, T. P. Robitaille, T. Spura, T. R. Jones, T. Cera, T. Leslie, T. Zito, T. Krauss, U. Upadhyay, Y. O. Halchenko, and Y. Vázquez-Baeza, "SciPy 1.0: fundamental algorithms for scientific computing in Python," Nat. Methods **17**(3), 261–272 (2020).